ACS NANO
Cite This: ACS Nano 2018, 12, 1887−1893
www.acsnano.org

ARTICLE

Few-Layer Antimonene: Anisotropic Expansion and Reversible Crystalline-Phase Evolution Enable Large-Capacity and Long-Life Na-Ion Batteries

Weifeng Tian,[†,#] Shengli Zhang,[§,#] Chengxue Huo,[§,#] Daming Zhu,[†] Qingwei Li,[†] Lei Wang,[†] Xiaochuan Ren,[†] Lei Xie,[†] Shiying Guo,[§] Paul K. Chu,[‖] Haibo Zeng,*[,§] and Kaifu Huo*[,†]

[†]Wuhan National Laboratory for Optoelectronics, School of Optical and Electronic Information, Huazhong University of Science and Technology, Wuhan 430074, China

[§]Institute of Optoelectronics & Nanomaterials, College of Materials Science and Engineering, Nanjing University of Science and Technology, Nanjing 210094, China

[‖]Department of Physics and Department of Materials Science, City University of Hong Kong, Tat Chee Avenue, Kowloon, Hong Kong, China

Supporting Information

ABSTRACT: **Two-dimensional (2D) antimonene is a promising anode material in sodium-ion batteries (SIBs) because of its high theoretical capacity of 660 mAh g^{-1} and enlarged surface active sites. However, its Na storage properties and sodiation/desodiation mechanism have not been fully explored. Herein, we propose the sodiation/desodiation reaction mechanism of 2D few-layer antimonene (FLA) based on results acquired by *in situ* synchrotron X-ray diffraction, *ex situ* selected-area electron diffraction, and theoretical simulations. Our study shows that the FLA undergoes anisotropic volume expansion along the *a*/*b* plane and exhibits reversible crystalline phase evolution (Sb ⇋ NaSb ⇋ Na_3Sb) during cycling. Density-functional theory calculations demonstrate that the FLA has a small Na-ion diffusion barrier of 0.14 eV. The FLA delivers a larger capacity of 642 mAh g^{-1} at 0.1 C (1 C = 660 mA g^{-1}) and a high rate capability of 429 mAh g^{-1} at 5 C and maintains a stable capacity of 620 mA g^{-1} at 0.5 C with 99.7% capacity retention from the 10th to the 150th cycle. Considering the 660 mAh g^{-1} theoretical capacity of Sb, the electrochemical utilization of Sb atoms of FLA is as high as 93.9% at a rate of 0.5 C for over 150 cycles, which is the highest capacity and Sb utilization ratio reported so far. Our study discloses the Na storage mechanism of 2D FLA, boosting promising applications of 2D materials for advanced SIBs.**

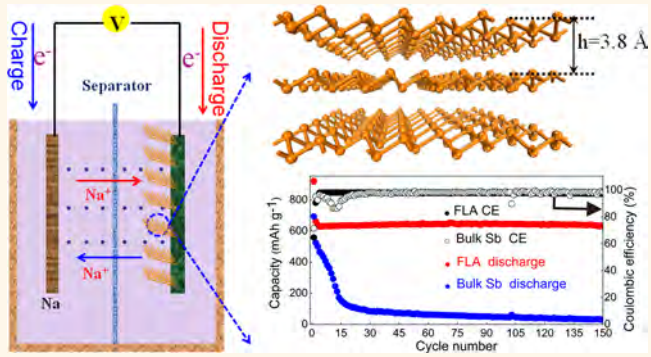

KEYWORDS: *few-layer antimonene, 2D materials, anisotropic expansion, reversible crystalline-phase evolution, sodium-ion batteries, large capacity*

The large demand for portable electronics, electronic vehicles, and large-scale power grid storage has spurred the development of advanced energy storage technologies and systems.[1,2] Among the various energy storage devices, room-temperature sodium-ion batteries (SIBs) have attracted increasing attention as alternatives to current lithium-ion batteries (LIBs) because sodium (Na) is abundant, economical, and readily available worldwide.[3] Since the performance of SIBs significantly depends on the Na storage capability of electrode materials, developing promising electrode materials with rational structures and surface properties is of great importance to promote the performance of SIBs.[4] Inspired by the large-capacity alloy anodes in LIBs, alloy-based anode materials for Na storage have attracted much attention lately.[5,6] In particular, antimony (Sb) is an appealing anode material for SIBs because of its large theoretical capacity of 660 mAh g^{-1} and low discharge potential of about 0.5 V (*vs* Na^+/Na).[7] Unfortunately, bulk Sb generally shows a quick capacity decay due to the severe pulverization as a result of the

Received: December 9, 2017
Accepted: January 25, 2018
Published: January 25, 2018

DOI: 10.1021/acsnano.7b08714
ACS Nano 2018, 12, 1887−1893

large volume changes of 390% during sodiation and desodiation processes.[8] This shortcoming has hitherto stifled widespread use of Sb and other alloy anode materials in SIBs. To solve this hurdle, several strategies have been developed to construct various Sb nanostructures, such as zero-dimensional (0D) porous and yolk−shell nanoparticles,[9,10] as well as one-dimensional (1D) nanomaterials[11] to mitigate the pulverization and cracking of Sb active materials. Recently, two-dimensional (2D) materials such as MoS_2,[12] VS_2,[13] ReS_2,[14] silicene,[15,16] and MXenes[17] have been studied as potential anodic materials in LIBs or SIBs, which exhibit enhanced electrochemical properties in terms of capacity, rate capability, and cycling performance compared to their bulk counterparts owing to the shorter diffusion path length for ion diffusion and enlarged surface active sites for ion storage.

2D antimonene, consisting of a buckled structure of hexagonal rings, has been recently predicted[18−20] and fabricated by mechanical exfoliation,[21] van der Waals epitaxy,[22,23] and liquid-phase exfoliation.[24] The large theoretical capacity of Sb and unique 2D features render few-layer antimonene (FLA) an appealing anode material for high-performance SIBs. However, the Na storage performance of 2D FLA has not been fully explored so far. Moreover, although Sb-based materials such as nanocrystals,[8] nanorods,[25] and nanocompositites[26] have been studied as anode materials in SIBs, the sodiation/desodiation mechanism of nanoscale Sb remains vague. In this regard, 2D FLA is ideally suited to unravel the sodiation/desodiation mechanism and maximize the Na storage performance.

In this work, we determine the superior Na storage properties of FLA and elucidate the sodiation/desodiation mechanism of FLA based on the results acquired *via in situ* synchrotron X-ray diffraction (XRD), *ex situ* selected-area electron diffraction (SAED), and density-functional theory (DFT) calculations. We demonstrate that FLA undergoes reversible crystalline phase evolution (Sb ⇋ NaSb ⇋ Na_3Sb) during cycles, and Na-ion alloying reactions proceed along the *a*/*b*-axis, resulting in in-plane anisotropic lattice expansion. Since the in-plane expansion along the *a*/*b* axial direction of 2D FLA is not constrained, FLA could achieve high structural stability for Na ion storage. These unexpected findings differ from previous reports in which bulk Sb is believed to undergo amorphorization during cycling.[27] DFT calculations indicate that 2D FLA has a small Na^+ diffusion barrier of 0.14 eV, which is much smaller than those of 2D MoS_2,[12] VS_2,[13] and silicene.[15] The reversible crystalline phase transformation, anisotropic volume change, and low Na ion diffusion barrier of FLA enable excellent Na storage performances. Galvanostatic studies demonstrate that 2D FLA delivers a large charging capacity of 642 mAh g^{-1} at 0.1 C (1 C = 660 mA g^{-1}) and a high rate capability of 429 mAh g^{-1} at a high current density of 5 C and maintains a stable capacity of 620 mAh g^{-1} at 0.5 C with 99.7% capacity retention from the 10th to the 150th cycle. Considering the 660 mAh g^{-1} theoretical capacity of Sb, the electrochemical utilization of Sb atoms is as high as 93.9% at a high rate of 0.5 C for over 150 cycles. They are the highest capacity and utilization ratio determined from alloy-based anodes reported so far (Table S1, Supporting Information). Our study reveals the Na storage mechanism of 2D FLA and provides strategies for the design and development of 2D materials for high-energy SIBs.

RESULTS AND DISCUSSION

The 2D FLA nanosheets are produced in a large quantity by liquid-phase exfoliation of *β*-antimony in 1:1 *N*-methyl pyrrolidone (NMP)/ethanol without any surfactant (see details in Methods). Figure 1a shows the schematic diagram of a Na-ion half-cell, in which FLA acts as the working electrode and Na foil as the counter electrode. The atomic model of FLA is schematically shown in Figure 1b, and the thickness of the as-synthesized FLA is measured *via* atomic force microscopy (AFM). Figure 1c,d are the typical AFM image and the corresponding line profile of FLA, demonstrating the thickness of FLA is about 7 nm (about 18 atomic layers). Figure S1 (Supporting Information) depicts the statistical analysis of 120 FLA flakes, showing that 78.3% FLA flakes have a thickness below 10 nm and 23.3% of flakes are thinner than 5 nm. The dimensions of as-synthesized FLA are about 200−1000 nm, as the AFM image indicates (Figure S1, Supporting Information). The XRD pattern acquired from the FLA flakes is similar to that of the *β*-Sb precursor (Figure S2, Supporting Information), but the full-width at half-maximum (FWHM) values of the (003) peak increase and the peak shifts to a small angle, suggesting a thinner FLA and expanded *c*-axis interlayer distance of the FLA compared to the bulk *β*-Sb precursor.[28,29]

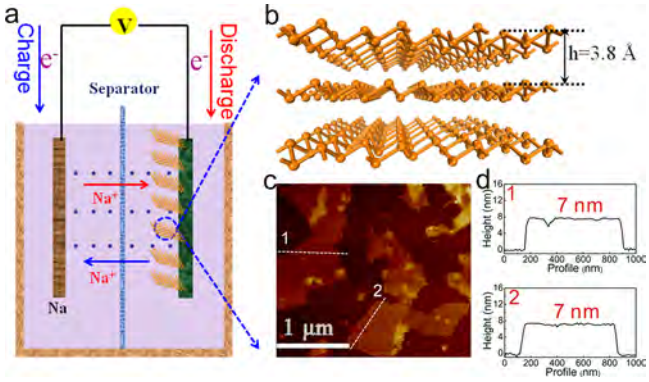

Figure 1. (a) Schematic diagram of the Na-ion half-cell composed of FLA. (b) Atomic structure illustration of FLA. (c) AFM image of FLA and (d) profile terraces of FLA.

The enlarged surface active sites and expanded *c*-axis interlayers of FLA enable large-capacity and fast sodiation reaction kinetics for SIBs as the following parts reveal.

The Raman scattering peaks (Figure S3a, Supporting Information) acquired from FLA are weaker compared to bulk *β*-Sb, and a similar decreasing trend with decreasing thickness is observed from the micromechanically exfoliated Sb flakes.[20] The A_{1g} and E_{1g} peaks of FLA are located at 154.0 and 116.8 cm^{-1}, respectively, showing blue-shifts to larger wavenumbers compared to bulk *β*-Sb probably because of the *c*-axis lattice expansion and in-plane lattice contraction.[21,23] X-ray photoelectron spectroscopy (XPS) reveals two peaks with binding energies of 537.4 and 528.0 eV, corresponding to $3d_{3/2}$ and $3d_{5/2}$ of metallic Sb[10,30] (Figure S4, Supporting Information). The transmission electron microscope (TEM) image (Figure S5a, Supporting Information) demonstrates that FLA is transparent, corroborating the thinner flake structure. The high-resolution TEM image (Figure S5b, Supporting Information) discloses a single-crystalline structure of FLA with a spacing of 0.216 nm corresponding to the (110) plane of *β*-Sb.

DOI: 10.1021/acsnano.7b08714
ACS Nano 2018, 12, 1887−1893

The 2D FLA exhibits good chemical stability, which is different from the same group 2D phosphorene that is unstable under ambient conditions.[31,32] After storing at atmospheric conditions for a month, the as-synthesized 2D FLA suspension (0.5 mg mL^{-1}) still exhibits a strong Tyndall effect (Figure S6, Supporting Information). X-ray energy dispersive spectrometry (EDS) confirms no obvious change in the chemical composition. The Raman peaks of A_{1g} and E_{1g} observed from the fresh FLA and FLA stored in atmospheric conditions for a month have no obvious change, and no additional Raman peaks of antimony oxide are observed as well (Figure S3b, Supporting Information), suggesting the high chemical stability of the as-synthesized FLA. These results indicate that stable 2D FLA could be produced in a large quantity by a facile liquid-phase exfoliation approach, which is crucial to the development of 2D antimonene technology for high-energy SIBs.

The electrochemical properties of the FLA anode are evaluated using CR2025-type coin-like cells as schematically shown in Figure 1a. The long-term cycles of FLA and the bulk Sb powder precursor are measured at a current density of 0.5 C (Figure 2a). Bulk Sb shows a quick capacity decay due to severe

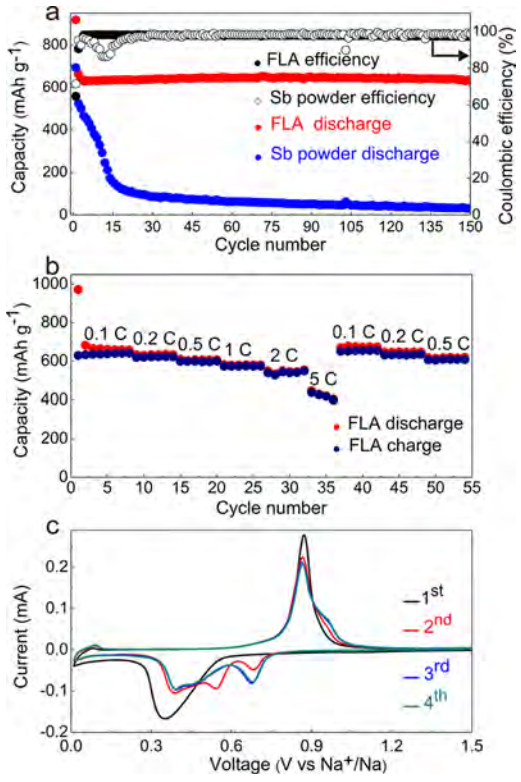

Figure 2. (a) Long-term cycling performance and Coulombic efficiency (CE) of the FLA and bulk Sb powder at a rate of 0.5 C. (b) Rate capability of FLA. (c) CV profiles of FLA between 0.01 and 1.5 V at a rate of 0.1 mV s^{-1}.

pulverization as a result of the large volume changes during the sodiation and desodiation processes.[8] However, the FLA electrode displays a stable capacity of 620 mAh g^{-1} at 0.5 C with 99.7% capacity retention from the 10th to the 150th cycle and a high Coulombic efficiency (CE) close to 100%. SEM images of FLA electrodes before and after 150 cycles are depicted in Figure S7a,b (Supporting Information), revealing no obvious morphology change. The 2D FLA could mitigate the pulverization and cracking of Sb, therefore demonstrating excellent cycle stability. Considering the theoretical capacity of 660 mAh g^{-1} for Sb, the large capacity of 620 mAh g^{-1} at 0.5 C means 93.9% of the Sb atoms in FLA take part in Na storage, even after 150 cycles. They are the highest capacity and Sb utilization ratio reported so far (see Table S1, Supporting Information). The initial CE of FLA is 64.7%, which is smaller than that of bulk Sb (71.5%). The larger irreversible capacity loss of the FLA electrode is attributed to a higher electrolyte/electrode surface area, which causes more side reactions with the electrolyte in the first cycling process. This phenomenon is also observed from nanostructured Si and Sb electrode materials.[8,33] Figure 2b demonstrates the rate capabilities of FLA. The FLA anode delivers a large capacity of 642 mAh g^{-1} at 0.1 C. When the current density is increased by 50 times to 5 C, a capacity of 429 mAh g^{-1} corresponding to 67% capacity retention is achieved. When the current density is returned to 0.1 C after 35 cycles, the specific capacity recovers to 645 mAh g^{-1}, thereby demonstrating good reversibility and high rate capability. The cyclic voltammograms (CVs) of the FLA anode are depicted in Figure 2c. They are acquired at a scanning rate of 0.1 mV s^{-1} in the voltage range from 0.01 to 1.5 V (*vs* Na^+/Na). During the first cathodic scan, a strong peak at 0.35 V is observed. In the second cycle, the three reduction peaks at 0.68, 0.55, and 0.39 V are identified and subsequently stabilized at 0.68 and 0.39 V, which correspond to the multistep Na−Sb alloying reactions from Sb to the intermediate NaSb phase and finally the Na_3Sb phase.[34] In the reverse anodic scan, the two anodic peaks at 0.88 and 0.96 V are associated with the desodiation reaction from Na_3Sb to NaSb and Sb, respectively. The peak current in the first cathodic scan is larger than those in the following ones due to decomposition of the electrolyte, forming solid state interface (SEI) layers on the FLA.[35] The CV scans overlap from the third cycle onward, indicating good reversibility and stability. Electrochemical impedance spectroscopy (EIS) and the corresponding equivalent circuit are presented in Figure S7c,d (Supporting Information). The charge transfer resistance (R_{ct}) at the electrode/electrolyte interface of the FLA anode in the 150th cycle is less than that in the first cycle, implying lower R_{ct} with cycles due to the slow wetting of the electrolyte and the activation of FLA electrodes, similar to Si anodes in LIBs.[36,37] Electrochemical studies (Figure 2) indicate that the 2D FLA delivers superior Na storage performance that surpasses those of previously reported Sb and alloy-based anodes (Table S1, Supporting Information).

To elucidate the Na storage mechanism of FLA, the sodiation/desodiation processes of FLA are monitored by SAED, *in situ* synchrotron XRD, and DFT calculations. The *ex situ* SAED images in the sodiation states at 1.5, 0.68, and 0 V and desodiation states at 0.96 and 1.5 V in the third cycle are depicted in Figure 3a. The SAED patterns at different voltages confirm the all the sodiated and desodiated samples are crystalline. The SAED patterns can be indexed to hexagonal Sb (JCPDS No. 35-0732), monoclinic NaSb (JCPDS No. 74-0801), and hexagonal Na_3Sb (JCPDS No. 04-0724). During the sodiation process, Na first reacts with Sb, forming crystalline NaSb at 0.68 V, and the Sb phase disappears. As sodiation continues, Na_3Sb is gradually formed at a discharging voltage of 0.39 V and becomes the major species relative to NaSb at a discharging voltage of 0.01 V. During the desodiation process, the crystalline Na_3Sb phase gradually transforms into the crystalline NaSb intermediate phase (0.96 V) and finally the Sb phase with a small account of NaSb (1.5 V). The existence of Sb and a small NaSb phase in the full sodiation and desodiation

DOI: 10.1021/acsnano.7b08714
ACS Nano 2018, 12, 1887−1893

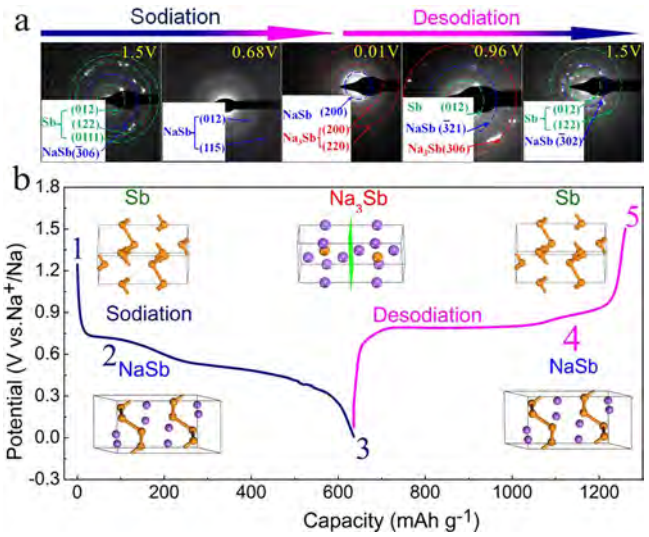

Figure 3. (a) *Ex situ* SAED patterns during sodiation at 1.5, 0.68, and 0.01 V and desodiation states at 0.96 and 1.5 V under a 0.5 C rate during the third discharging/charging cycle. (b) Schematic diagram showing the five states of the FLA anode during sodiation/desodiation processes corresponding to the different crystalline phases/crystal structures of Sb, NaSb, and Na_3Sb at the specific charging−discharging voltage.

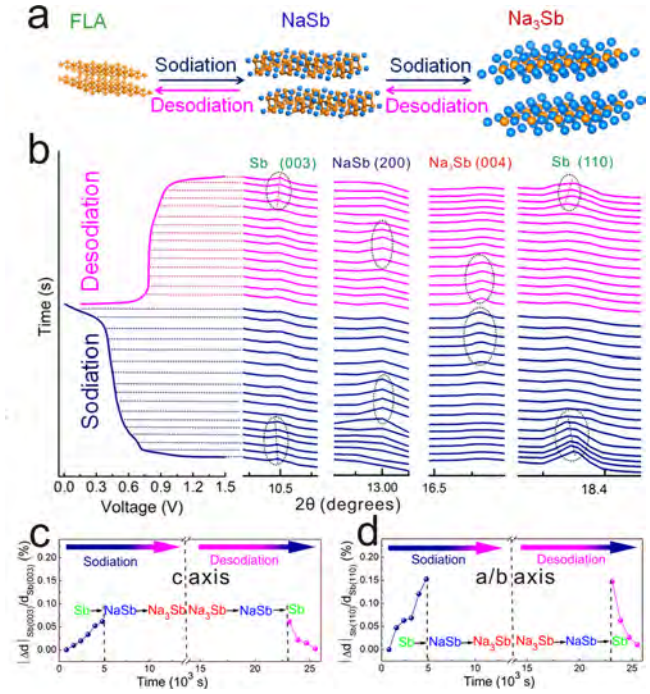

Figure 4. (a) Schematic diagram of the crystalline phase evolution(Sb ⇋ NaSb ⇋ Na_3Sb) during the sodiation/desodiation process. (b) *In situ* XRD pattern evolution of FLA anodes during the third sodiation/desodiation process at a current of 0.2 C. (c, d) Change of Sb lattice constants of (003) and (110) planes corresponding to the *c*-axis and *a*/*b*-axis during sodiation/desodiation processes.

states is attributed to incomplete sodiation/desodiation reactions at a large current density of 0.5 C. The *ex situ* SAED patterns are consistent with CV curves (Figure 2c), in which the four peaks in the CV curves are attributed to the five sequential sodiation/desodiation transformations of Sb → NaSb → Na_3Sb → NaSb → Sb during cycling, which are schematically illustrated in Figure 3b.

The above results indicate that the FLA anode undergoes a reversible crystalline-phase transformation of Sb ⇋ NaSb ⇋ Na_3Sb during cycling, as depicted in Figure 4a. To further reveal the lattice change in FLA during cycling, we conduct *in situ* synchrotron XRD during the third cycle as shown in Figure 4b. The FLA peaks of (003) and (110) planes both shift to smaller angles during the initial sodiation processes, and then the two diffraction peaks attenuate. Meanwhile, the diffraction peaks of NaSb and Na_3Sb successively appear. In the reverse desodiation process, the two peaks of NaSb and Na_3Sb fade away and the Sb peaks of (003) and (110) planes enhance with the desodiation. Moreover, the FLA peaks of the (003) and (110) planes both shift to larger angles. These results clearly support the crystalline-phase transformation (Sb → NaSb → Na_3Sb → NaSb → Sb) during cycling, which is consistent with *ex situ* SAED results (Figure 3a). Compared to the (003) peak, the angle changes of the (110) peak are larger during the sodiation and desodiation processes, suggesting larger expansion along the (110) plane (*a*/*b* axial direction) during sodiation processes. The detailed lattice changing rates of $\Delta d(003)/d(003)$ (*c*-axis) and $\Delta d(110)/d(110)$ (*a*/*b*-axis) are presented in Figure 4c,d. The slight increase in the *c* lattice parameter along the (003) direction during initial sodiation is attributed to Na-ion insertion between layers of FLA. The larger lattice expansion along the (110) plane (*a*/*b*-axis) may stem from in-plane (*a*/*b*-axis) alloying reactions forming crystalline NaSb and Na_3Sb alloys. The interlayer distance of FLA is about 3.8 Å, which could accommodate the large Na^+ ions.[38] Therefore, Na^+ insertion between the layers in FLA does not significantly alter the *c* axial lattice parameter. The inserted Na^+ ions further react with Sb atoms to produce crystalline NaSb and finally Na_3Sb, resulting in in-plane lattice expansion along the *a*/*b*-axis. Figure 4c,d clearly reveal that the lattice expansion of the (110) planes is almost 3 times larger than that of the (003) plane, confirming anisotropic volume expansion along the *a*/*b*-axis during sodiation reactions. For the 2D FLA, since the in-plane expansion along the *a*/b axial direction is not constrained, it can accommodate the larger anisotropic volume change along the *a*/*b*-axis during the Sb ⇋ NaSb ⇋ Na_3Sb transformation to achieve high structural stability for Na ion storage.

To further evaluate the sodiation and desodiation process of FLA, we further studied Na adsorption and diffusion properties on monolayer antimonene by using first-principles calculations. Three possible adsorption sites of Na are shown in Figure S8 (Supporting Information). The top site is above the higher Sb atom, the hollow site is above the middle of a hexagonal ring, and the valley site is above the lower Sb atom. Optimization results show that the Na adsorption is an exothermic process and the valley adsorption system is the most stable. We also explore the diffusion path and barrier between two adjacent valley sites by the complete LST/QST method. The results are illustrated in Figure 5a,b. The calculated energy barrier for Na diffusion is 0.14 eV, which is smaller than those of 2D MoS_2 (0.28 eV),[15] VS_2 (0.22 eV),[13] silicene (0.24 eV),[12] and graphene (0.22 eV).[39] The low Na-ion diffusion barrier and slight *c*-axial lattice parameter expansion enable fast Na-ion diffusion. Furthermore, the DFT results in Figure 5c also confirm the larger lattice expansion along the *a*/*b*-axis direction compared to the *c*-axis from the Sb phase to Na_3Sb. Our study suggests that storage of Na ions in FLA proceeds by Na-ion fast

DOI: 10.1021/acsnano.7b08714
ACS Nano 2018, 12, 1887−1893

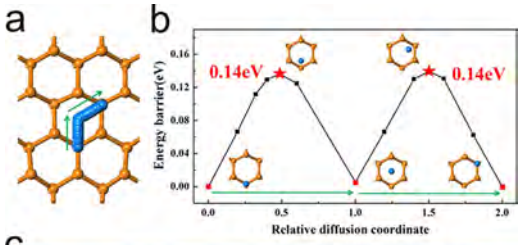

bulk	a(Å)	b(Å)	c(Å)	Volume(Å³)	Volume(Å³) (Sb_{24})	V/V_{Sb}
Sb (Sb_6)	4.39	4.39	11.45	190.38	761.52	1
NaSb (Na_8Sb_8)	6.83	6.41	12.59	489.08	1467.24	1.93
Na_3Sb (Na_6Sb_2)	5.37	5.37	9.56	239.29	2847.48	3.74

Figure 5. (a) Optimal Na diffusion pathway. (b) Calculated barriers for Na-ion diffusion in FLA. (c) Calculated changes in the lattice parameters and volume during the sodiation/desodiation process (Sb ⇋ NaSb ⇋ Na_3Sb).

diffusion and alloying reactions forming crystalline NaSb and Na_3Sb alloys along the *a*/*b*-axis, which provide clear structural correlation with the excellent Na storage property.

CONCLUSION

In summary, the 2D FLA is an appealing anode material for Na storage, which shows a large capacity of 620 mAh g^{-1} after 150 charging/discharging cycles at 0.5 C, corresponding to a 93.9% utilization ratio, and a high rate capability of 429 mAh g^{-1} at 5 C. Storage of Na ions in FLA is believed to proceed through Na^+ insertion followed by in-plane alloying reactions along the *a*/*b*-axis. The 2D FLA allows fast Na ion diffusion with a small diffusion barrier of 0.14 eV. We demonstrate that 2D FLA can accommodate the anisotropic volume change along the *a*/*b*-axis and reversible crystalline-phase evolution (Sb ⇋ NaSb ⇋ Na_3Sb) during cyclings to achieve high structural stability and fast electrochemical redox kinetics for Na-ion storage. The anisotropic volume expansion, reversible crystalline phase evolution, and low Na-ion diffusion barrier of FLA enable long-life, large-capacity, and high rate-capability SIBs. Our results elucidate the Na storage mechanism of 2D FLA and provide strategies for the development of high-performance 2D materials in advanced metal-ion batteries.

METHODS

Materials Synthesis. The 2D few-layer antimonene was fabricated by the ultrasonic treatment of antimony powders in an *N*-methylpyrrolidinone/ethanol mixture at 200 W for 5−6 h. Afterward, the mixture was centrifuged at 3000 rpm to remove the unexfoliated Sb, and a dark gray suspension consisting of few-layer antimonene was obtained. To obtain the FLA sample, the suspension was centrifuged at 8000 rpm, rinsed with ethanol, and then freeze-dried under vacuum. The concentration of FLA in NMP/ethanol is measured by weighing the FLA suspension and dried FLA *via* removing the NMP/ethanol solution.

Characterization. The morphology, structure, and composition of the samples were characterized by field-emission scanning electron microscopy (FE-SEM, Nano SEM 450), transmission electron microscopy (Tecnai G20), energy-dispersive X-ray spectroscopy (Oxford INCA 200), X-ray diffraction (Philips X'Pert Pro), Raman scattering (HR RamLab, 532 nm), and X-ray photoelectron spectroscopy (AXIS-ULTRA DLD-600W). The thickness of FLA was determined by atomic force microscopy (Bruker Multimodel-8).

Electrode Fabrication and Electrochemical Tests. The electrochemical performance of FLA was evaluated using coin-like 2025 cells assembled in an argon-filled glovebox. To prepare the electrodes, the active materials, carbon black, and carboxymethyl cellulose (CMC) were mixed at a ratio of 65:20:15, and water was added dropwise to form a slurry. The slurry was put on a copper foil and vacuum-dried at 60 °C overnight. The mass loading of the FLA electrode was about 1.0 mg cm^{-2}. The Na metal acted as the counter electrode, and glass fiber (Whatman) served as the separator. The electrolyte was 1 M $NaClO_4$ in ethylene carbonate (EC) and diethyl carbonate (DEC) with 5 wt % fluoroethylene carbonate (FEC) as an additive.

Electrochemical Measurements. Cyclic voltammetry (CV) was performed on an electrochemical workstation (CHI 660E, Shanghai, China) at a scanning rate of 0.1 mV s^{-1} between 0.01 and 1.5 V *versus* Na^+/Na. Electrochemical impedance spectroscopy was conducted on the same instrument at frequencies between 100 kHz and 0.01 Hz with an amplitude of 5 mV. The galvanostatic charging−discharging tests were carried out on an Xinwei instrument (Shenzhen, China), and the cutoff voltage was varied from 0.01 to 1.5 V *versus* Na^+/Na. The specific capacities were calculated on the basis of the mass of the active FLA, and all the electrochemical tests were performed at room temperature.

***Ex Situ* SAED.** The coin-like 2025 cells at sodiation states of 1.5, 0.68, and 0 V and desodiation states of 0.96 and 1.5 V under a 0.5 C rate were disassembled in an argon-filled glovebox. Then, the FLA electrodes were first immersed in DEC and then in anhydrous ethanol several times. Finally, the electrodes were ultrasonically treated and the suspension of the FLA was dropped on a carbon-coated copper grid for TEM (Tecnai G20) and SAED characterizations.

***In Situ* Synchrotron XRD.** The *in situ* synchrotron XRD data were acquired on the Beamline BL148 (18 keV, 0.06887 nm) at the Shanghai Synchrotron Radiation Facility with an image plate detector in the transmission mode.[40,41] The freestanding electrode film was composed of the active materials, carbon black, and CMC at a ratio of 65:20:15. A sodium plate as the counter electrode had a hole punched in the center for the penetrating synchrotron beam, 1 M $NaClO_4$ in EC/DEC as the electrolyte, and a Walkman glass fiber as the separator. Mylar film, stainless steel, and a sealing washer were used to assemble the *in situ* cell in an argon-filled glovebox. Discharging and charging of the cell was carried out on a Land BT2000 battery test system (Wuhan, China) between 0.01 and 1.5 V *versus* Na^+/Na at a current rate of 0.2 C.

Computational Methods. The theoretical derivation was carried out using DFT implemented in the DMol3 package.[42−44] The Perdew−Burke−Ernzerhof functional was used in the GGA as implemented in the DMol3 package. The electronic eigenfunctions were expanded in terms of a localized atomic orbital basis set of double numerical plus polarization DNP quality. A 4 × 4 × 1 supercell was used to simulate Na adsorption on the monolayered antimonene. The calculation included a DFT-D correction using the Grimme method. A vacuum space of about 20 Å between antimonene layers was used to avoid any interactions. The convergence criteria of energy and force were set to 1 × 10^{-5} Ha and 0.002 Ha/Å, and the displacement was 0.005 Ha. The atomic distance cutoff in real space was set as "Fine", and the transition state search used complete LST/QST as a search protocol. The convergence tolerance was set to "Fine" quality, and the RMS convergence was set to 0.002 eV/Å.

ASSOCIATED CONTENT

Supporting Information

The Supporting Information is available free of charge on the ACS Publications website at DOI: 10.1021/acsnano.7b08714.

Height profile of AFM images, thickness statistics bar chart, XRD pattern, Raman spectra, XPS spectrum, SEM, HR-TEM, EDS mapping, EIS data and the corresponding equivalent circuit, adsorption sites and Na-ion diffusion on the surface of the antimonene (PDF)

DOI: 10.1021/acsnano.7b08714
ACS Nano 2018, 12, 1887−1893

AUTHOR INFORMATION

Corresponding Authors

*E-mail: zeng.haibo@njust.edu.cn.
*E-mail: kfhuo@hust.edu.cn.

ORCID

Haibo Zeng: 0000-0002-0281-3617
Kaifu Huo: 0000-0001-5670-8233

Author Contributions

#W. Tian, S. Zhang, and C. Huo contributed equally to this work.

Notes

The authors declare no competing financial interest.

ACKNOWLEDGMENTS

We thank the Shanghai Synchrotron Radiation Facility (SSRF) BL14B1 staff. This work was financially supported by National Natural Science Foundation of China (NSFC, Nos. 51572100, 61434001, 51504171, and 51572128), the Natural Science Foundation of Hubei Province (No. 2015CFA116), the Director Fund of WNLO, the Fundamental Research Funds for the Central Universities (HUST: 2015QN071), the National Basic Research Program of China (2014CB931702), NSFC-RGC (5151101197), PAPD of Jiangsu Higher Education Institutions, and City University of Hong Kong Applied Research Grant (ARG) Nos. 9667122 and 9667144. The authors also thanks the Nanodevices and Characterization Center of HUST-WNLO and Analytical and Testing Center of HUST.

REFERENCES

(1) Shi, Y.; Zhou, X.; Yu, G. Material and Structural Design of Novel Binder Systems for High Energy, High-Power Lithium-Ion Batteries. *Acc. Chem. Res.* **2017**, *50*, 2642−2652.

(2) Hoshide, T.; Zheng, Y.; Hou, J.; Wane, Z.; Li, Q.; Zhao, Z.; Ma, R.; Sasaki, T.; Geng, F. Flexible Lithium-Ion Fiber Battery by the Regular Stacking of Two Dimensional Titanium Oxide Nanosheets Hybridized with Reduced Graphene Oxide. *Nano Lett.* **2017**, *17*, 3543−3549.

(3) Luo, W.; Shen, F.; Bommier, C.; Zhu, H.; Ji, X.; Hu, L. Na-Ion Battery Anodes: Materials and Electrochemistry. *Acc. Chem. Res.* **2016**, *49*, 231−240.

(4) Liu, Y.; Zhang, A.; Shen, C.; Liu, Q.; Cao, X.; Ma, Y.; Chen, L.; Lau, C.; Chen, T.-C.; Wei, F.; Zhou, C. Red Phosphorus Nanodots on Reduced Graphene Oxide as a Flexible and Ultra-Fast Anode for Sodium-Ion Batteries. *ACS Nano* **2017**, *11*, 5530−5537.

(5) Sheng, T.; Xu, Y.; Jiang, Y.; Huang, L.; Tian, N.; Zhou, Z.; Broadwell, I.; Sun, S. Structure Design and Performance Tuning of Nanomaterials for Electrochemical Energy Conversion and Storage. *Acc. Chem. Res.* **2016**, *49*, 2569−2577.

(6) Palomares, V.; Serras, P.; Villaluenga, I.; Hueso, K.-B.; Carretero-Gonzálezb, J.; Rojo, T. Na-Ion Batteries, Recent Advances and Present Challenges to Become Low Cost Energy Storage Systems. *Energy Environ. Sci.* **2012**, *5*, 5884−5901.

(7) Liu, J.; Yang, Z.; Wang, J.; Gu, L.; Maier, J.; Yu, Y. Three-dimensionally Interconnected Nickel-antimony Intermetallic Hollow Nanospheres as Anode Material for High-Rate Sodium-Ion Batteries. *Nano Energy* **2015**, *16*, 389−398.

(8) Zhao, Y.; Manthiram, A. High-Capacity, High-Rate Bi-Sb Alloy Anodes for Lithium-Ion and Sodium-Ion Batteries. *Chem. Mater.* **2015**, *27*, 3096−3101.

(9) Hou, H.; Jing, M.; Yang, Y.; Zhang, Y.; Zhu, Y.; Song, W.; Yang, X.; Ji, X. Sb Porous Hollow Microspheres as Advanced Anode Materials for Sodium-Ion Batteries. *J. Mater. Chem. A* **2015**, *3*, 2971−2977.

(10) Wang, N.; Bai, Z.; Qian, Y. T.; Yang, J. One-Dimensional Yolk-Shell Sb@Ti-O-P Nanostructures as A High Capacity and High-Rate Anode Material for Sodium Ion Batteries. *ACS Appl. Mater. Interfaces* **2017**, *9*, 447−454.

(11) Liu, Z.; Yu, X.; Lou, X.; Paik, U. Sb@C Coaxial Nanotubes as A Superior Long-life and High-Rate Anode for Sodium Ion Batteries. *Energy Environ. Sci.* **2016**, *9*, 2314−2318.

(12) Mortazavi, M.; Wang, C.; Deng, J.; Shenoy, V.-B.; Medhekar, N.-V. *Ab Initio* Characterization of Layered MoS_2 as Anode for Sodium-Ion Batteries. *J. Power Sources* **2014**, *268*, 279−286.

(13) Jing, Y.; Zhou, Z.; Cabrera, C.-R.; Chen, Z. Metallic VS_2 Monolayer: A Promising 2D Anode Material for Lithium Ion Batteries. *J. Phys. Chem. C* **2013**, *117*, 25409−25413.

(14) Zhang, Q.; Wang, W.; Kong, X.; Mendes, R.-G.; Fang, L.; Xue, Y.; Xiao, Y.; Rümmeli, M.-H.; Chen, S.; Fu, L. Edge-to-Edge Oriented Self-Assembly of ReS_2 Nanoflakes. *J. Am. Chem. Soc.* **2016**, *138*, 11101−11104.

(15) Zhuang, J.; Xu, X.; Peleckis, G.; Hao, W.; Dou, S.; Du, Y. Silicene: A Promising Anode for Lithium-Ion Batteries. *Adv. Mater.* **2017**, *1606716*, 1−8.

(16) Tritsaris, G.-A.; Kaxiras, E.; Meng, S.; Wang, E. Adsorption and Diffusion of Lithium on Layered Silicon for Li-Ion Storage. *Nano Lett.* **2013**, *13*, 2258−2263.

(17) Kajiyama, S.; Szabova, L.; Sodeyama, K.; Iinuma, H.; Morita, R.; Gotoh, K.; Tateyama, Y.; Okubo, M.; Yamada, A. Sodium-Ion Intercalation Mechanism in MXene Nanosheets. *ACS Nano* **2016**, *10*, 3334−3341.

(18) Zhang, S.; Yan, Z.; Li, Y.; Chen, Z.; Zeng, H. Atomically Thin Arsenene and Antimonene: Semimetal-Semiconductor and Indirect-Direct Band-Gap Transitions. *Angew. Chem., Int. Ed.* **2015**, *54*, 3112−3115.

(19) Zhang, S.; Xie, M.; Li, F.; Yan, Z.; Li, Y.; Kan, E.; Liu, W.; Chen, Z.; Zeng, H. Semiconducting Group 15 Monolayers: A Broad Range of Band Gaps and High Carrier Mobilities. *Angew. Chem.* **2016**, *128*, 1698−1701.

(20) Persson, K.; Hinuma, Y.; Meng, Y.-S.; Van der Ven, A.; Ceder, G. Thermodynamic and Kinetic Properties of the Li-Graphite from First-Principles Calculations. *Phys. Rev. B: Condens. Matter Mater. Phys.* **2010**, *82*, 125416.

(21) Ares, P.; Aguilar-Galindo, F.; Rodriguez-San-Miguel, D.; Aldave, D.-A.; Diaz-Tendero, S.; Alcamí, M.; Martín, F.; Gomez-Herrero, J.; Zamora, F. Mechanical Isolation of Highly Stable Antimonene Under Ambient Conditions. *Adv. Mater.* **2016**, *28*, 6332−6336.

(22) Ji, J.; Song, X.; Liu, J.; Yan, Z.; Huo, C.; Zhang, S.; Su, M.; Liao, L.; Wang, W.; Ni, Z.; Hao, Y.; Zeng, H. Two-Dimensional Antimonene Single Crystals Grown by Van Der Waals Epitaxy. *Nat. Commun.* **2016**, *7*, 13352.

(23) Wu, X.; Shao, Y.; Liu, H.; Feng, Z.; Wang, Y.; Sun, J.; Liu, C.; Wang, J.; Liu, Z.; Zhu, S. Epitaxial Growth and Air-Stability of Monolayer Antimonene on $PdTe_2$. *Adv. Mater.* **2017**, *29*, 1605407.

(24) Gibaja, C.; Rodriguez-San-Miguel, D.; Ares, P.; Gomez-Herrero, J.; Varela, M.; Gillen, R.; Maultzsch, J.; Hauke, F.; Hirsch, A.; Abellán, G.; Zamora, F. Few-Layer Antimonene by Liquid-Phase Exfoliation. *Angew. Chem., Int. Ed.* **2016**, *55*, 1−6.

(25) Liang, L.; Xu, Y.; Wang, C.; Wen, L.; Fang, Y.; Mi, Y.; Zhou, M.; Zhao, H.; Lei, Y. Large-Scale Highly Ordered Sb Nanorod Array Anodes with High Capacity and Rate Capability for Sodium-Ion Batteries. *Energy Environ. Sci.* **2015**, *8*, 2954−2962.

(26) Qian, J.; Chen, Y.; Wu, L.; Cao, Y.; Ai, X.; Yang, H. High Capacity Na-Storage and Superior Cyclability of Nanocomposite Sb/C Anode for Na-Ion Batteries. *Chem. Commun.* **2012**, *48*, 7070−7072.

(27) Darwiche, A.; Marino, C.; Sougrati, M.; Fraisse, B.; Stievano, L.; Monconduit, M. Better Cycling Performances of Bulk Sb in Na-Ion Batteries Compared to Li-Ion Systems: an Unexpected Electrochemical Mechanism. *J. Am. Chem. Soc.* **2012**, *134*, 20805−20811.

(28) Huh, S. X-ray Diffraction of Multi-Layer Graphenes: Instant Measurement and Determination of the Number of Layers. *Carbon* **2014**, *78*, 617−621.

DOI: 10.1021/acsnano.7b08714
ACS Nano 2018, 12, 1887−1893

(29) Zhu, D.; Gao, H.; Zhang, X.; Yang, T.; Li, L.; Yin, G.; Li, X.; Nicklin, C.; Gao, X.; Li, Z.; Yi, L.; Li, X. Real-Time Observation of Graphene Layer Growth: Coupling of the Interlayer Spacing with Thickness. *Carbon* **2015**, *94*, 775−780.
(30) Wang, N.; Bai, Z.; Qian, Y.; Yang, J. Double-Walled Sb@TiO_{2-x} Nanotubes as A Superior High-Rate and Ultralong-Lifespan Anode Material for Na-Ion and Li-Ion Batteries. *Adv. Mater.* **2016**, *28*, 4126−4133.
(31) Island, J.-O.; Steele, G. A.; Van der Zant, H.; Castellanos-Gomez, A. Environmental Instability of Few-Layer Black Phosphorus. *2D Mater.* **2014**, *2*, 011002.
(32) Sinha, S.; Takabayashi, Y.; Shinohara, H.; Kitaura, R. Simple Fabrication of Air-Stable Black Phosphorus Heterostructures with Large-Area hBN Sheets Grown by Chemical Vapor Deposition Method. *2D Mater.* **2016**, *3*, 035010.
(33) Bruce, P.-G.; Scrosati, B.; Tarascon, J.-M. Nanomaterials for Rechargeable Lithium Batteries. *Angew. Chem., Int. Ed.* **2008**, *47*, 2930−2946.
(34) Kong, B.; Zu, L.; Peng, C.; Zhang, Y.; Zhang, W.; Tang, J.; Selomulya, C.; Zhang, L.; Chen, H.; Wang, Y.; Liu, Y.; He, H.; Wei, J.; Lin, X.; Luo, W.; Yang, J.; Zhao, Z.; Liu, Y.; Yang, J.; Zhao, D. Direct Superassemblies of Freestanding Metal-Carbon Frameworks Featuring Reversible Crystalline-Phase Transformation for Electrochemical Sodium Storage. *J. Am. Chem. Soc.* **2016**, *138*, 16533−16541.
(35) Wang, L.; Gao, B.; Peng, C.; Peng, X.; Fu, J.; Chu, P.; Huo, K. Bamboo Leaf Derived Ultrafine Si Nanoparticles and Si/C Nanocomposites for High-Performance Li-Ion Battery Anodes. *Nanoscale* **2015**, *7*, 13840−13847.
(36) Lv, R.; Yang, J.; Wang, J.; NuLi, Y. Electrodeposited Porous-Microspheres Li-Si Films as Negative Electrodes in Lithium-Ion Batteries. *J. Power Sources* **2011**, *196*, 3868−3873.
(37) Wu, H.; Yu, G.; Pan, L.; Liu, N.; McDowell, M.-T.; Bao, Z.; Cui, Y. Stable Li-Ion Battery Anodes by *In-Situ* Polymerization of Conducting Hydrogel to Conformally Coat Silicon Nanoparticles. *Nat. Commun.* **2013**, *4*, 1943.
(38) Wen, Y.; He, K.; Zhu, Y.; Han, F.; Xu, Y.; Matsuda, I.; Cumings, J.; Wang, C. Expanded Graphite as Superior Anode for Sodium-Ion Batteries. *Nat. Commun.* **2014**, *5*, 4033.
(39) Persson, K.; Hinuma, Y.; Meng, Y.-S.; Van der Ven, A.; Ceder, G. Thermodynamic and Kinetic Properties of the Li-Graphite from First-Principles Calculations. *Phys. Rev. B: Condens. Matter Mater. Phys.* **2010**, *82*, 125416.
(40) Zhu, D.; Liu, X.; Gao, Y.; Li, Y.; Wang, R.; Xu, Z.; Ji, G.; Jiang, S.; Zhao, B.; Yin, G.; Li, L.; Yang, T.; Wang, Y.; Yi, L.; Li, X. *In Situ* Observation of Thermal Proton Transport through Graphene Layers. *ACS Nano* **2017**, *11*, 8970−8977.
(41) Zhu, D.; Liu, H.; Tai, L.; Zhang, X.; Jiang, S.; Yang, S.; Yi, L.; Wen, W.; Li, X. Facile Construction of Novel 3-Dimensional Graphene/Amorphous Porous Carbon Hybrids with Enhanced Lithium Storage Properties. *ACS Appl. Mater. Interfaces* **2017**, *9*, 35191−35199.
(42) Ordejón, P.; Artacho, E.; Soler, J. Self-Consistent Order-N Density-Functional Calculations for Very Large Systems. *Phys. Rev. B: Condens. Matter Mater. Phys.* **1996**, *53*, R10441−10443.
(43) Sánchez-Portal, D.; Portal, D.; Ordejón, P.; Artacho, E.; Soler, J. Density-Functional Method for Very Large Systems with LCAO Basis Sets. Systems with LCAO Basis Sets. *Int. J. Quantum Chem.* **1997**, *65*, 453−461.
(44) Delley, B. DMOL3 Is A Density Functional Theory Program Distributed by Accelrys. *J. Chem. Phys.* **1990**, *92*, 508−517.

DOI: 10.1021/acsnano.7b08714
ACS Nano 2018, 12, 1887−1893

Supporting Information

Few-Layer Antimonene: Anisotropic Expansion and Reversible Crystalline-Phase Evolution Enable Large-Capacity and Long-Life Na-Ion Batteries

Weifeng Tian [†,#] *Shengli Zhang,* [§,#] *Chengxue Huo,* [§,#] *Daming Zhu,* [†] *Qingwei Li,* [†] *Lei Wang,* [†] *Xiaochuan Ren,* [†] *Lei Xie,* [†] *Shiying Guo,* [§] *Paul K Chu,* [‖] *Haibo Zeng,* [*,§] *and Kaifu Huo*[*,†]

[†]Wuhan National Laboratory for Optoelectronics, School of Optical and Electronic information, Huazhong University of Science and Technology, Wuhan 430074, China

[§]Institute of Optoelectronics & Nanomaterials, College of Materials Science and Engineering, Nanjing University of Science and Technology, Nanjing 210094, China

[‖]Department of Physics and Materials Science, City University of Hong Kong, Tat Chee Avenue, Kowloon, Hong Kong, China

[#]These authors contributed equally to this work.

* Corresponding author: zeng.haibo@njust.edu.cn; kfhuo@hust.edu.cn

Figures

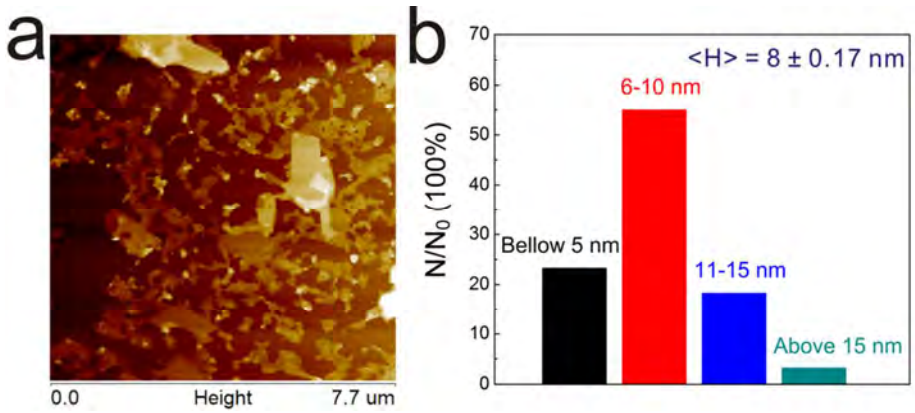

Figure S1 (a) AFM image of FLA nanosheets on SiO_2 /Si substrate. (b) The height analysis of various sizes FLA samples (sample size =120), and the mean thickness of FLA is 8 ± 0.17 nm.

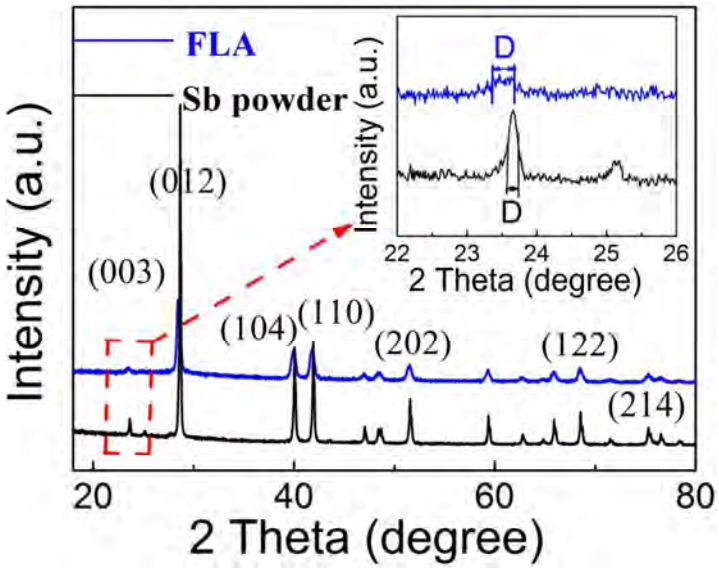

Figure S2 XRD pattern of the β-phase Sb powder and as-synthesized FLA, and the inset is the half peak width magnification of (003).

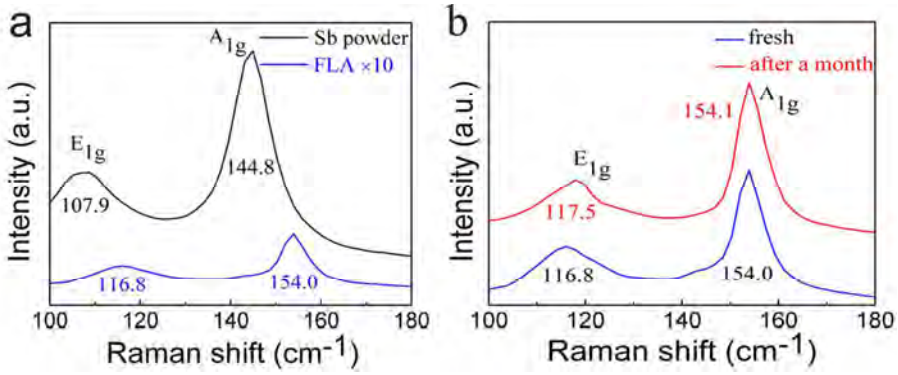

Figure S3 (a) Raman spectra of the FLA and Sb powder. (b) Raman spectra of both fresh FLA and FLA stored atmospheric conditions after a month.

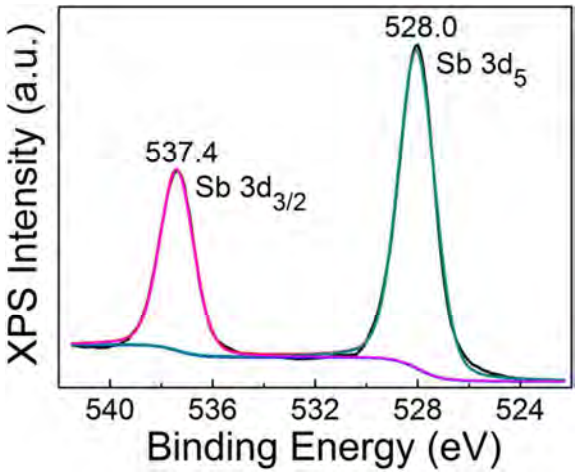

Figure S4 XPS spectrum of as-synthesized FLA.

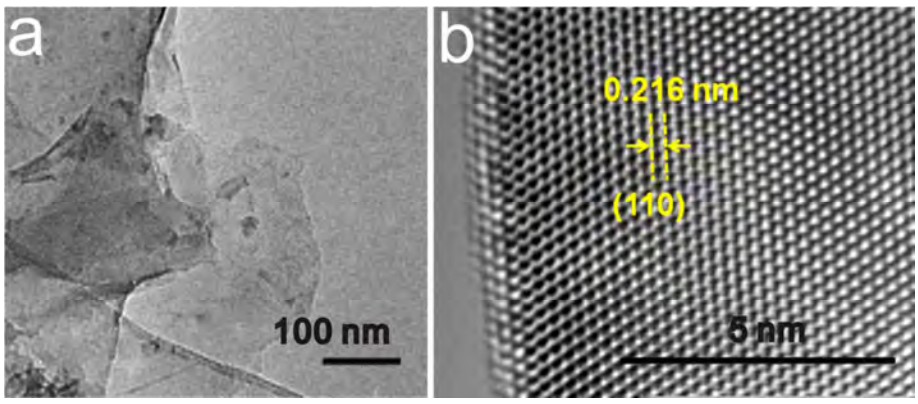

Figure S5 (a) TEM image of the FLA nanoflakes (scale bar: 100 nm). (**b**) HR-TEM image of the FLA (scale bar: 5 nm).

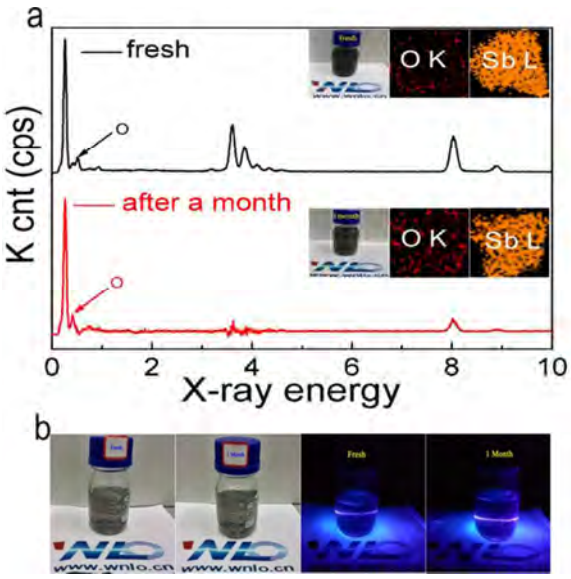

Figure S6 (a) EDS analysis of the fresh and aged (stored atmospheric conditions for 30 days) FLA and the insets are the optical photograph and elemental maps of O and Sb (FLA concentration is about 2 mg ml^{-1}). (b) Photographs of the freshly exfoliated FLA and aged (stored atmospheric conditions for 30 days) dispersions showing the Faraday-Tyndall effect (after the dilute concentration is about 0.5mg ml^{-1}).

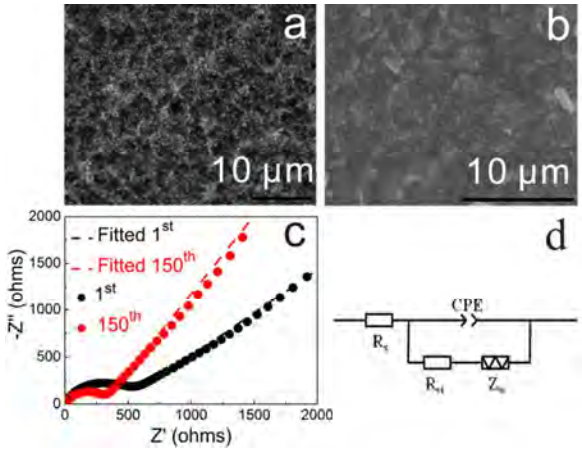

Figure S7 (a) and (b) are the SEM images of the fresh FLA electrode and after 150 cycles (scale bar: 10μm). (c) EIS and fitted curve of FLA electrode after 1st and 150th charging and discharging cycles. (d) Corresponding equivalent circuit diagram (R_s, R_{ct} and Z_w are contact resistance, charge-transfer resistance and Warburg impedance, respectively, and CPE is constant phase element).

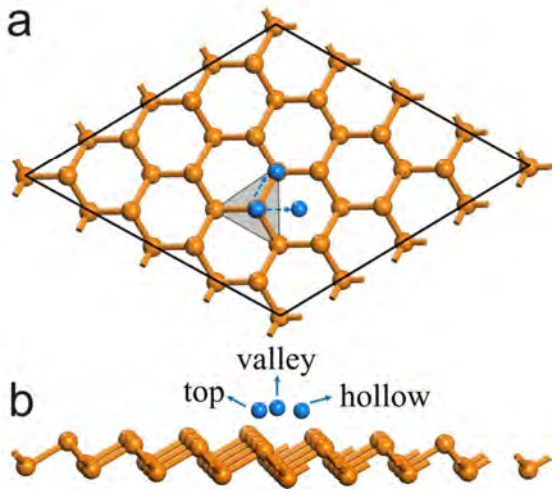

Figure S8 Adsorption sites for sodium ion diffusion on the surface of the FLA.

Table S1. A summary of recent results obtained from alloy-based anode materials for sodium-ion batteries.

Electrode materials	Current density ($mA\ g^{-1}$)	Cycle	Capacity ($mAh\ g^{-1}$)	Utilization
Bulk Sb[1]	330	80	576	87.2%
Sb Nanocrystals[2]	660	100	500 (10 nm)	75.8%
			580 (20nm)	87.8%
Nanoporous-antimony[3]	100	200	573.8	86.9%
leaf-like Sb[4]	500	150	589	89.2%
Sb film[5]	66	2	525	79.5%
Sb@C nanotubes[6]	100	240	407	61.7%
Sb/C nanocomposite[7]	2000	100	573	86.9%
Sb/TiO_2 nanocomposite[8]	2640	1000	300	45.5%
Sb porous hollow Microspheres[9]	100	100	600	90.9%
Electrospun Sb/C Fibers[10]	100	300	350	53.0%
Sb–C nanofibers[11]	200	400	450	68.2%
Bi nanorod[12]	50	150	302	79.5%
Porou Sn[13]	424	500	519	61.3%
Sn nanodots@ C microcages[14]	20	300	332	39.2%
TiO_2-Sn@Carbon[15]	100	400	413	48.8%
Sn nanoparticles @ carbon[16]	847	1000	390	46%
Yolk−shell Sn@C[17]	2000	800	430	50.8%
amorphous phosphorus[18]	15	80	1000	38.5%
Black Phosphorus[19]	125	23	1573	60.1%
Amorphous Phosphorus/ Nitrogen-Doped Graphene[20]	350	1500	809	31.2%
Our work (FLA)	**330**	**150**	**620**	**93.9%**

References

(1) Darwiche, A.; Marino, C.; Sougrati, M.; Fraisse, B.; Stievano, L.; Monconduit, L. Better Cycling Performances of Bulk Sb in Na-Ion Batteries. Compared to Li-Ion Systems: An Unexpected Electrochemical Mechanism. *J. Am. Chem. Soc.* **2012,** *134*, 20805–20811.

(2) He, M.; Kravchyk, K.; Walter, M.; Kovalenko, M. Monodisperse Antimony Nanocrystals for High-Rate Li-Ion and Na Ion Battery Anodes: Nano *versus* Bulk. *Nano Lett*. 2014, *14*, 1255–1262.

(3) Liu, S.; Feng, J.; Bian, X.; Liu, J.; Xu, H. Morphology-Controlled Synthesis of Nanoporous-Antimony Anode for High-Performance Sodium-Ion Batteries. *Energy Environ. Sci.* **2016**, *9*, 1229–1236.

(4) Liang, L.; Xu, Y.; Li, Y.; Dong, H.; Zhou, M.; Zhao, H.; Kaiser, U.; Lei, Y. Facile Synthesis of Hierarchical Fern Leaf-Like Sb and Its Application as Additive-Free Anode for Fast Reversible Na-Ion Storage. *J. Mater. Chem. A* **2017**, *5*, 1749–1755.

(5) Baggetto, L.; Ganesh, P.; Sun, C.-N.; Meisner, R.-A.; Zawodzinski, T.-A; Veith, G.-M.; Intrinsic Thermodynamic and Kinetic Properties of Sb Electrodes for Li-Ion and Na-Ion Batteries: Experiment and Theory. *J. Mater. Chem. A* **2013**, *1*, 7985–7994.

(6) Liu, Z.; Yu, X.; Lou, X.; Paik, U. Sb@C Coaxial Nanotubes as A Superior Long-Life and High-Rate Anode for Sodium Ion Batteries. *Energy Environ. Sci.* **2016**, *9*, 2314–2318.

(7) Qian, J.; Chen, Y.; Wu, L.; Cao, Y.; Ai, X.; Yang, H. High Capacity Na-Storage and Superior Cyclability of Nanocomposite Sb/C Anode for Na-Ion Batteries. *Chem. Commun.* **2012**, *48*, 7070–7072.

(8) Wang, N.; Bai, Z.; Qian, Y.; Yang, J. Double-Walled Sb@TiO_{2-x} Nanotubes as A Superior High-Rate and Ultralong-Lifespan Anode Material for Na-Ion and Li-Ion Batteries. *Adv. Mater.* **2016**, *28*, 4126–4133.

(9) Hou, H.; Jing, M.; Yang,Y.; Zhang, Y.; Zhu, Y.; Song, W.; Yang, X.; Ji, X. Sb Porous Hollow Microspheres as Advanced Anode Materials for Sodium-Ion Batteries. *J. Mater. Chem. A* **2015**, *3*, 2971–2977.

(10) Zhu, Y.; Han, X.; Xu, Y.; Liu, Y.; Zheng, S.; Xu, K.; Hu, L.; Wang, C. Electrospun Sb/C Fibers for a Stable and Fast Sodium-Ion Battery Anode. *ACS. Nano* **2013**, *7*, 6378–6386.

(11) Wu, L.; Hu, X.; Qian, J.; Pei, F,; Wu, F.; Mao, R.; Ai, X.; Yang, H.; Cao, Y. Sb-C Nanofibers with Long Cycle Life as An Anode Material for High-Performance Sodium-Ion Batteries. *Energy Environ. Sci.* **2014**, *7*, 323–328.

(12) Liu, S.; Feng, J.; Bian, X.; Liu, J.; Xu, H. Advanced Arrayed Bismuth Nanorod Bundle Anode for Sodium-Ion Batteries. *J. Mater. Chem. A* **2016**, *4*, 10098–10104.

(13) Kim, C.; Lee, K.-Y.; Kim, I.; Park, J.; Cho, G.; Kim, K.-W.; Ahn, J.-H.; Ahn, H.-J. Long-Term Cycling Stability of Porous Sn Anode for Sodium-Ion Batteries. *Journal of Power Sources* **2016**, *317*, 153–158.

(14) Ying, H.; Zhang, S.; Meng, Z.; Sun, Z.; Han, W. Ultrasmall Sn Nanodots Embedded inside N-doped Carbon Microcages as High-Performance Lithium and Sodium Ion Battery Anodes. *J. Mater. Chem. A* **2017**, *5*, 8334–8342.

(15) Mao, M.; Yan, F.; Cui, C; Ma, J.; Zhang, M.; Wang, T.; Wang, C. Pipe-Wire TiO_2-Sn@Carbon Nanofibers Paper Anodes for Lithium and Sodium Ion Batteries. *Nano Lett.* **2017**, *13*, 2258–2263.

(16) Sha, M.; Zhang, H.; Nie, Y.; Nie, K.; Lv, X.; Sun, N.; Xie, X.; Ma, Y.; Sun, X. Sn Nanoparticles @ Nitrogen-doped Carbon Nanofiber Composites as High-Performance Anodes for Sodium-Ion Batteries. *J. Mater. Chem. A* **2017**, *5*, 6277–6283.

(17) Li, S. Wang, Z; Liu, J.; Yang, L.; Guo, Y.; Cheng, L.; Lei, M.; Wang, W. Yolk-shell Sn@C Eggette-Like Nanostructure: Application in Lithium-Ion and Sodium-Ion Batteries. *ACS Appl. Mater. Interfaces* **2016**, *8*, 19438–19445.

(18) Qian, J.; Wu, X.; Cao, Y.; Ai, X.; Yang, H. High Capacity and Rate Capability of Amorphous Phosphorus for Sodium Ion Batteries. *Angew. Chem.* **2013**, *125*, 4731–4734.

(19) Dahbi, M.; Yabuuchi, N.; Fukunishi, M.; Kubota, K.; Chihara, K.; Tokiwa, K.; Yu, X.; Ushiyama, H.; Yamashita, K.; Son, J. Son, J.-Y.; Cui, Y.-T.; Oji, H.; Komaba, S. Chem. Mater. Black Phosphorus as A High-Capacity, High-Capability Negative Electrode for Sodium-Ion Batteries: Investigation of The Eelectrode/Electrolyte Interface. *Chem. Mater.* **2016**, *28*, 1625–1635.

(20) Zhang, C.; Wang, X.; Liang, Q.-F.; Liu, X.-Z.; Weng, Q.-H.; Liu, J.-W.; Yang, Y.-J.; Dai, Z.-H.; Ding, K.-J.; Bando, Y.; Tang, J.; Golberg, D. Amorphous Phosphorus/Nitrogen-Doped Graphene Paper Forultrastable Sodium-Ion Batteries. *Nano Lett.* **2016**, *16*, 2054–2060.